

Enhanced electron-phonon coupling in doubly aligned hexagonal boron nitride bilayer graphene heterostructure

Manabendra Kuri,¹ Saurabh Kumar Srivastav¹,¹ Sujay Ray,¹ Kenji Watanabe²,² Takashi Taniguchi,² Tanmoy Das,¹ and Anindya Das^{1,*}

¹*Department of Physics, Indian Institute of Science, Bangalore 560012, India*

²*National Institute of Material Science, 1-1 Namiki, Tsukuba 305-0044, Japan*



(Received 24 November 2020; revised 17 February 2021; accepted 24 February 2021; published 12 March 2021)

The relative twist angle in heterostructures of two-dimensional materials with similar lattice constants results in a dramatic alteration of the electronic properties. Here, we investigate the electrical and magnetotransport properties in bilayer graphene encapsulated between two hexagonal boron nitride (hBN) crystals, where the top and bottom hBN are rotationally aligned with the bilayer graphene with a twist angle $\theta_t \sim 0^\circ$ and $\theta_b < 1^\circ$, respectively. This results in the formation of two moiré superlattices, with the appearance of satellite resistivity peaks at carrier densities n_{s1} and n_{s2} , in both hole- and electron-doped regions, together with the resistivity peak at zero carrier density. Furthermore, we measure the temperature (T) dependence of the resistivity (ρ). The resistivity shows a linear increment with temperature within the range 10 to 50 K for the density regime $n_{s1} < n < n_{s2}$ with a large slope $d\rho/dT \sim 8.5 \Omega/\text{K}$. The large slope of $d\rho/dT$ is attributed to the enhanced electron-phonon coupling arising due to the suppression of Fermi velocity in the reconstructed minibands, which was theoretically predicted recently in doubly aligned graphene with top and bottom hBN. Our result establishes the ability of the doubly aligned moiré system to tune the strength of electron-phonon coupling and to modify the electronic properties of multilayered heterostructures.

DOI: [10.1103/PhysRevB.103.115419](https://doi.org/10.1103/PhysRevB.103.115419)

I. INTRODUCTION

Rotational alignment between atomically thin two-dimensional (2D) crystals leads to the artificial superlattice potential forming moiré patterns [1]. One well-established example is graphene on hexagonal boron nitride (hBN). The weak periodic potential due to the underlying hBN gives rise to modulation of the graphene electronic band structure [2–4], with the emergence of clone Dirac cones [5], wherein the Fermi velocity could be controlled by the relative twist angle between the graphene and hBN, showing interesting physics such as the Hofstadter butterfly [6], resonant tunneling [7], change of topological winding number [8], topological valley current [9], and Brown-Zak oscillations [10]. Moreover, twisting individual layers leads to flat bands [11], where emergent phenomena such as correlated insulating state [12], superconductivity [13], quantum anomalous Hall effect [14], Chern insulating states [15,16], moiré excitons [17], and ferromagnetism [14] have been observed. Furthermore, in multilayered heterostructures, a competing moiré superlattice could be present due to the lattice mismatch between individual layers which can lead to further dramatic change in the electronic properties [18,19].

Alternatively, another concomitant way to engineer a moiré superlattice is to exploit the rotational alignment of graphene with both top and bottom hBN. This could result in two moiré superlattice structures of wavelength λ_t and λ_b ,

respectively. The interference of these two moiré superlattices could result in a supermoiré structure of wavelength λ_r . The supermoiré wavelength λ_r can vary from ~ 1 nm to infinity, depending on the rotational alignment of graphene with top (bottom) hBN [18]. Recently, the transport measurements have been carried out for hBN/graphene/hBN doubly aligned heterostructures and the signature of supermoiré patterns has been observed [19]. Furthermore, in Ref. [20], it has been theoretically predicted that the band is less dispersive with reduced Fermi velocity for the minibands in doubly aligned hBN/graphene/hBN heterostructures. Since the bilayer graphene (BLG) has a parabolic dispersion, it is expected to exhibit a further reduction in Fermi velocity in doubly aligned hBN/BLG/hBN heterostructures as compared to the monolayer counterpart. However, there are no experimental studies of these kinds of structures.

Here, we study the low-temperature electrical transport in a hBN/BLG/hBN heterostructure, where the top and bottom hBN are rotationally aligned with BLG with a twist angle $\theta_t \sim 0^\circ$ and $\theta_b < 1^\circ$, respectively. The low-temperature transport shows the emergence of additional satellite resistivity peaks at carrier densities (n_{s1} , n_{s2}) in hole- as well as electron-doped regions, together with the intrinsic resistivity peak at zero carrier density. The Hall resistance at low magnetic field shows an expected sign change at these peak positions. Furthermore, we study the temperature dependence of resistivity as a function of carrier density. We find that resistivity (ρ) varies with temperature as $\sim \rho_0(n) + AT^\beta$ for different carrier densities. Interestingly, we find that in the density regime $n_{s1} < n < n_{s2}$,

*anindya@iisc.ac.in

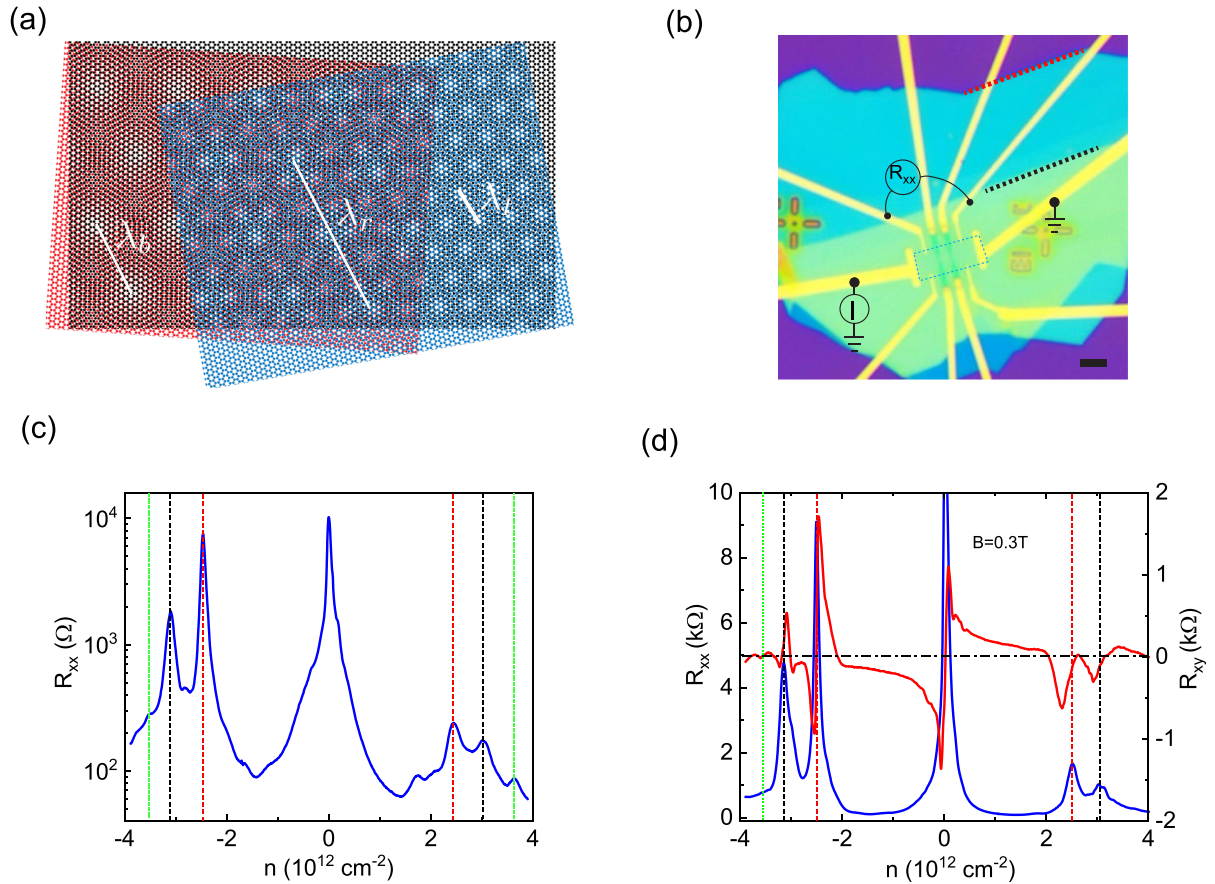


FIG. 1. (a) Schematic illustration of the moiré superlattice. Bilayer graphene (black) is encapsulated between the top (bottom) hBN marked with blue (red), respectively. (b) Optical image of the device with the measurement scheme. The edge of the top (bottom) hBN is marked with a black (red) dashed line. Scale bar $\sim 2 \mu\text{m}$. (c) Four-terminal resistance (R_{xx}) as a function of carrier density (n) measured at $T \sim 250$ mK. The red (black) vertical dashed lines correspond to SDP1 (SDP2), and the green dotted line corresponds to one of the supermoiré peaks. (d) Hall resistance R_{xy} and longitudinal resistance R_{xx} , as a function of carrier density for $B = 0.3$ T. The Hall resistance changes sign at PDP, SDP1, and SDP2, indicating that the Fermi energy crosses the superlattice band. Similarly, Hall resistance also changes sign near $n \sim -3.6 \times 10^{12} \text{ cm}^{-2}$, which corresponds to one of the supermoiré wavelengths.

the measured resistivity varies linearly ($\beta \sim 1$) with temperature within the range 10 to 50 K. The slope of resistivity ($d\rho/dT$) in this linear regime was found to be a maximum of $\sim 8.5 \Omega/\text{K}$. This value is approximately two orders of magnitude higher than pristine graphene with $d\rho/dT \sim 0.1 \Omega/\text{K}$ [21–23]. The linear dependence of resistivity with temperature arises due to the electron-acoustic phonon scattering [23,24]. It was recently shown theoretically in Ref. [20] that in doubly aligned hBN/graphene/hBN heterostructures, the minibands are less dispersive with reduced Fermi velocity in the density regime $n_{s1} < n < n_{s2}$. In our device, we attribute the higher value of $d\rho/dT$ to the enhanced electron-phonon coupling resulting from the suppression of Fermi velocity in these minibands.

II. RESULTS AND DISCUSSION

We fabricated bilayer graphene (BLG) devices encapsulated between two hexagonal boron nitride crystals using the dry transfer technique [25–27]. The fabrication technique is similar to our earlier work [4,27,28]. In addition, the BLG edge was carefully aligned with the crystallographic axes

of both top (bottom) hBN. The natural rectangular shape of bilayer graphene allowed us to pattern the device into a Hall bar geometry. Edge contacts were established by standard electron-beam lithography followed by thermal deposition of Cr/Pd/Au (2/10/70 nm). The optical image of the device is shown in Fig. 1(b). The measurements were carried out in a ^3He cryostat using the standard lock-in technique, in a four-terminal configuration, as schematically shown in Fig. 1(b).

Figure 1(a) shows the illustration of the appearance of a moiré pattern, where the two crystals, BLG and hBN, are aligned relative to one another (θ_t with top hBN, and θ_b with bottom hBN). The relative rotation between the two crystals defines the moiré wavelength λ_i . The appearance of a supermoiré structure has been illustrated in Fig. 1(a). In our device, the top hBN is nearly perfectly aligned with bilayer graphene ($\theta_t \sim 0^\circ$), whereas the bottom hBN has a slightly different twist angle ($\theta_b \leq 1^\circ$). Figure 1(c) shows the four-terminal longitudinal resistance as a function of carrier density (n) at $T \sim 250$ mK. The estimated mobility of our device was found to be $\mu \sim 57000 \text{ cm}^2/\text{Vs}$ (see Supplemental Material [29]). In addition to the resistance peak at the primary Dirac point (PDP), we also observe two strong resistance peak

at $n_{s1} \sim -2.46 \times 10^{12} \text{ cm}^{-2}$ and $n_{s2} \sim -3.09 \times 10^{12} \text{ cm}^{-2}$, highlighted by red and black dashed vertical lines in Fig. 1(c), respectively. The resistance peaks corresponding to densities n_{s1} and n_{s2} originate due to the two different moiré superlattice potentials arising from the rotational alignment of top and bottom hBN with BLG. We attribute the satellite resistance peaks corresponding to densities n_{s1} , n_{s2} as secondary Dirac point 1 (SDP1) and secondary Dirac point 2 (SDP2), respectively. It was reported that the second satellite peak (SDP2) may appear even in a single aligned graphene/hBN heterostructure due to the formation of a Kekule superstructure with $n_{s2} \sim 1.65n_{s1}$ [30]. However, for our device, $n_{s2} \sim 1.2n_{s1}$. Thus, we rule out the origin of SDP2 due to the formation of a Kekule superstructure. It is worthwhile to mention here that the spatial distribution of the twist angles over the sample should be uniform to observe the strong side resistivity peaks.

In contrast to the strong resistance peak in the hole-doped regime, weak resistance peaks are observed in the electron-doped regime, at similar densities. This asymmetry in electron-hole transport in BLG/hBN moiré devices arises because the hBN induces different on-site energies, which is stronger for the hole band as compared to the electron band [2,20,31]. The electron-hole asymmetry has also been observed experimentally [2,19] and calculated theoretically [20] for monolayer graphene aligned with two hBN, citing a similar origin. Now, from the carrier density of the satellite peak, we can estimate the moiré wavelength (λ_i) given by $n_s = 8/\sqrt{3}\lambda_i^2$. The resistance peak corresponding to carrier density n_{s1} shows a perfect alignment of BLG with top hBN ($\theta_t \sim 0.0^\circ$) with a moiré wavelength of $\lambda_t \sim 13.7 \text{ nm}$. Similarly, the resistance peak at n_{s2} corresponds to a moiré wavelength of $\lambda_b \sim 12.2 \text{ nm}$ ($\theta_b \sim 0.56^\circ$). The interference of these two moiré superlattices could result in the formation of a supermoiré structure. In Ref. [20], the supermoiré wavelengths have been theoretically calculated based on four possible reciprocal lattice vector configurations. For our device, $\theta_t \sim 0.0^\circ$ and $\theta_b \sim 0.56^\circ$, the possible supermoiré wavelengths are $\sim 25.6, 23.4, 11.7,$ and 9.3 nm (see Supplemental Material [29]). The resistance peaks observed in our experiment at $n \sim \pm 3.6 \times 10^{12} \text{ cm}^{-2}$ [marked as a green dotted line in Fig. 1(c)] corresponds to a moiré wavelength of $\sim 11.5 \text{ nm}$, which closely matches with one of the supermoiré wavelengths (11.7 nm). However, a weak shoulder at $n \sim \pm 1.9 \times 10^{12} \text{ cm}^{-2}$ does not match with any supermoiré wavelength. In Ref. [19], it was proposed that these peaks could be due to more exotic superlattice phenomena or higher-order moiré periodicities. Figure 1(d) shows the Hall resistance R_{xy} as a function of carrier density for a perpendicular magnetic field of $B = 0.3 \text{ T}$. As one would expect, the charge carriers change from holelike to electronlike when crossing both the charge neutrality $n = 0$ and superlattice gaps for n_{s1} and n_{s2} . We would also like to note that the Hall resistance changes sign at $n \sim -3.6 \times 10^{12} \text{ cm}^{-2}$, which corresponds to the supermoiré wavelength of $\sim 11.7 \text{ nm}$, highlighted by a green dotted vertical line in Fig. 1(d).

III. MAGNETIC FIELD DATA

We measure the Hall resistance R_{xy} and the longitudinal resistance R_{xx} as a function of a perpendicular magnetic

field (B) and carrier density (n). We observe quantum oscillations evolving from PDP, SDP1, and SDP2 for both the electron and hole sides. Figure 2(a) shows the measured R_{xx} as a function of carrier density and magnetic field for both electron- and hole-doped regions. The sequence of R_{xy} verifies that indeed our flake is bilayer graphene (see Supplemental Material [29]). Alternatively, we extract the Shubnikov-de Haas (SdH) oscillation frequency (f_{SdH}), from which we can calculate the Landau level (LL) degeneracy for $n = 0$ and for n_{s1} , n_{s2} [12]. The SdH oscillation frequency is given by $f_{SdH} = \phi_0 |n|/S$, where S represents the degeneracy of the Landau levels. In BLG, due to the spin and valley degeneracy, $S = 4$. Figure 2(b) shows the measured oscillation frequency as a function of carrier density. Near PDP, we obtain $S = 4$, revealing the observed fillings at $\nu = \pm 4, \pm 8, \pm 12, \dots$, consistent with the LL spectrum of intrinsic bilayer graphene. Similarly, the LL fan for n_{s1} and n_{s2} also has a degeneracy of $S = 4$.

IV. TEMPERATURE DEPENDENCE

The dependence of the material's resistivity with temperature reveals important physics related to carrier scattering, electron-phonon coupling, and electron-electron interactions in the system [32]. Figure 3(a) shows the 2D color plot of $R_{xx}(T)$ as a function of carrier density (n). Insulating behavior was observed at PDP, SDP1, and SDP2. Figure 3(b) shows the line cut of Fig. 3(a) at several temperatures. It can be seen that the resistivity increases with the increase in temperature close to $n \sim -2.8 \times 10^{12} \text{ cm}^{-2}$ in between SDP1 and SDP2, signifying metallic transport. Figure 3(c) shows the Arrhenius plot $\rho(T)$ vs $1/T$ at PDP, SDP1, and SDP2. Activated transport is observed for PDP and SDP1. However, although the SDP2 shows activated behavior at low temperature, the resistivity increases at high temperatures. The linear fit with the Arrhenius equation gives a gap of $\Delta_{n_{s1}} \sim 3 \text{ meV}$ and $\Delta_{n_{s2}} \sim 1.2 \text{ meV}$ for SDP1 and SDP2, respectively. In Fig. 3(d), we show ρ with T , for several values of n between n_{s1} and n_{s2} . We see that ρ evolves linearly with T up to $T \sim 50 \text{ K}$. We fit our temperature dependence data in the range of 10 to 50 K with $\rho(n, T) \sim \rho_0(n) + AT^\beta$. We find that in the region $n_{s1} < n < n_{s2}$, $\rho(n, T) \sim \rho_0 + AT$ with $\beta \sim 1$, and a maximum value of A is found to be $A = d\rho/dT \sim 8.5 \text{ } \Omega/\text{K}$. In Fig. 3(e), we show the ρ - T for a few other densities. It can be seen in Fig. 3(e) that in the region between PDP and SDP1, β reaches up to ~ 1.9 . Close to PDP, resistivity increases nonmonotonically with temperature, as can be seen in the inset of Fig. 3(e).

The value of $d\rho/dT$ in the regime $n_{s1} < n < n_{s2}$ is nearly two orders of magnitude larger compared to intrinsic monolayer graphene with $d\rho/dT \sim 0.1 \text{ } \Omega/\text{K}$ [21–23]. It is worthwhile to mention here that the resistivity of intrinsic bilayer graphene shows a very weak dependence on temperature [33,34]. In Fig. 3(f), we plot β as a function of carrier density. It can be seen that $\beta \sim 1$, in the region $n_{s1} < n < n_{s2}$, in the hole-doped region. Qualitatively similar behavior was observed in the electron-doped regime with a smaller value of $d\rho/dT \sim 0.9 \text{ } \Omega/\text{K}$ (see Supplemental Material [29]). However, at all other densities, β changes significantly with the change in carrier densities, as can be seen in Fig. 3(f). Recently, it has been shown theoretically [20] that in

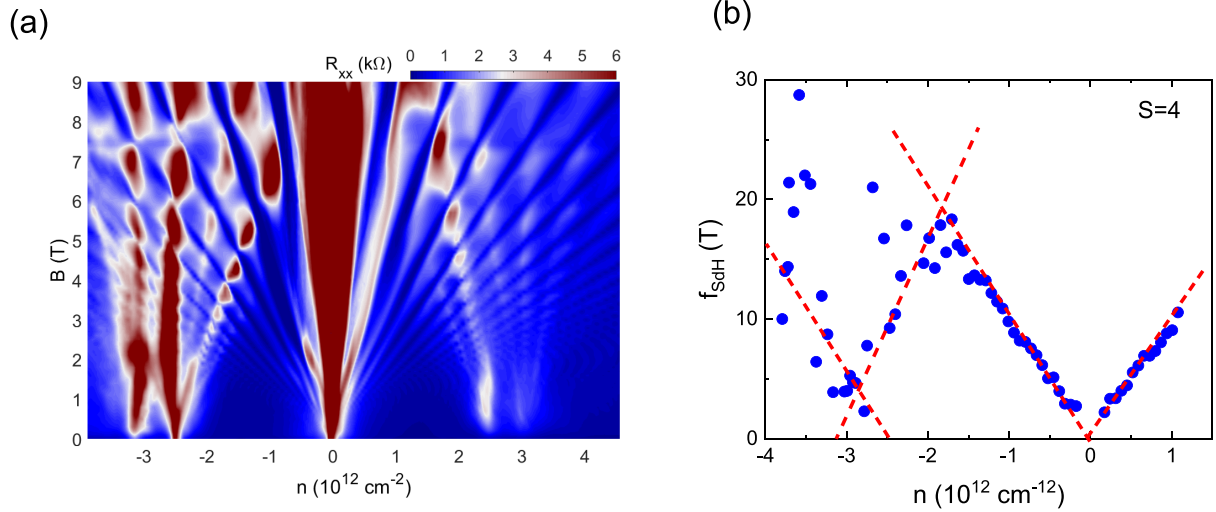


FIG. 2. (a) Landau fan diagram as a function of the perpendicular magnetic field (B) and carrier density (n) at $T \sim 250$ mK. Quantum oscillations are observed at PDP with $\nu = 4, 8, 12, \dots$ and also with SDP1 and SDP2 with fillings $\nu = 4$ evolving from n_{s1} . (b) Extracted SdH oscillation frequency as a function of carrier density obtained from (a).

the doubly aligned hBN/graphene/hBN heterostructures, the reconstruction of the band structures gives rise to the formation of less dispersive minibands with reduced Fermi velocity. Now, having BLG in our device over monolayer could imply

a further reduction in the Fermi velocity since the low-energy dispersion is parabolic in BLG. Thus, one expects a further reduction in Fermi velocity for hBN/BLG/hBN heterostructures. This could give rise to large electron-phonon coupling

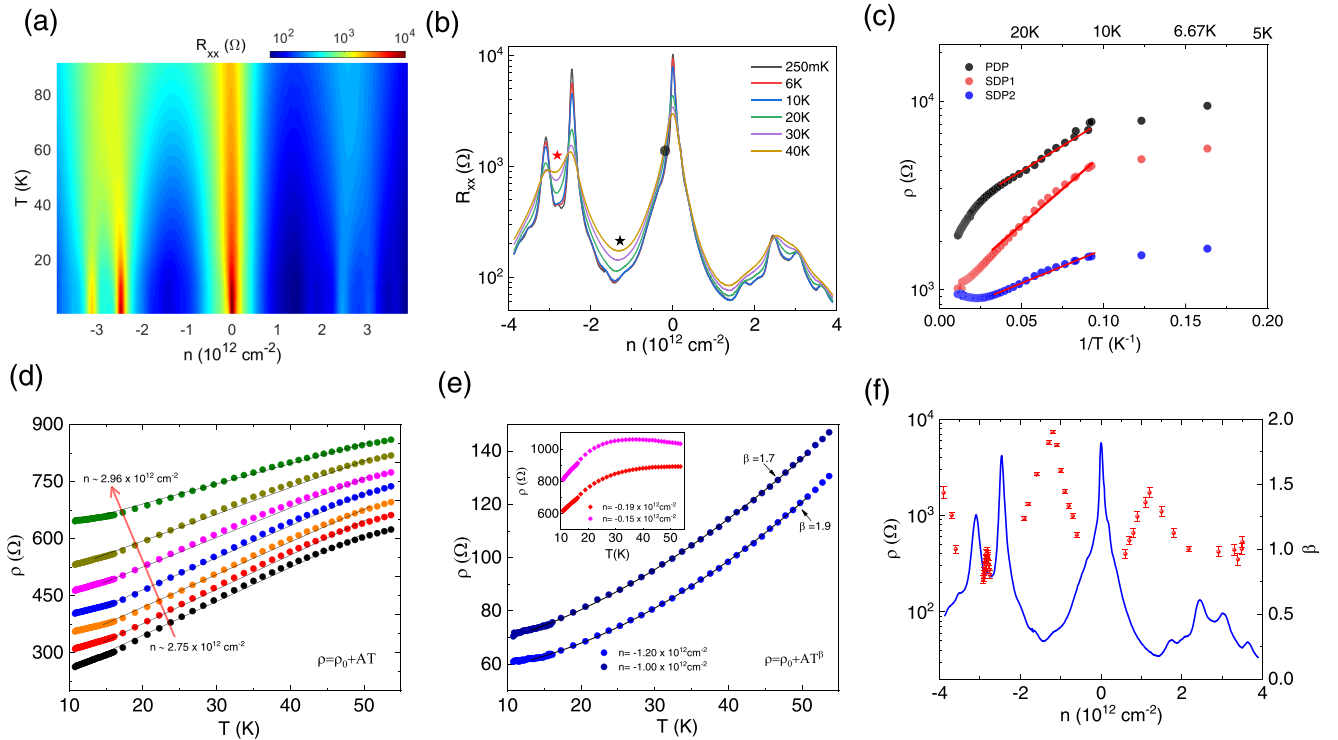


FIG. 3. (a) Four-terminal resistance as a function of carrier density, for several values of temperature from $T \sim 250$ mK to 90 K. (b) Line traces of resistance vs carrier density from (a) for $T \sim 250$ mK, 6 K, 10 K, 20 K, 30 K, and 40 K. (c) Arrhenius plot of resistivity ρ vs $1/T$ at PDP, SDP1, and SDP2, showing activated transport behavior, yielding a gap $\Delta_{SDP1} \sim 3$ meV and $\Delta_{SDP2} \sim 1.2$ meV. The dashed line shows the linear fit. (d) ρ vs T for several values of n in the range $n_{s1} < n < n_{s2}$, highlighted as a red star in (b). The solid lines show the fit with $\rho \sim \rho_0(n) + AT$, for the temperature range for 10 to 50 K, with a slope of $A = d\rho/dT \sim 8.5$ Ω/K . (e) ρ with T for a few other values of carrier densities highlighted as a black star in (b). The solid lines are the fit with $\rho \sim \rho_0(n) + AT^\beta$. Inset: the ρ vs T for the region marked as a black circle in (b). (f) ρ and β as a function of carrier density.

similar to what has been observed in twisted bilayer graphene devices [35]. Due to this enhanced electron-phonon coupling, we observe the large $d\rho/dT$ of $\sim 8.5 \Omega/\text{K}$ in the density regime $n_{s1} < n < n_{s2}$. To compare our results with monolayer graphene, we follow the similar approach that was used for monolayer graphene and twisted bilayer graphene. Theoretically, the resistivity at high T , due to acoustic phonon-induced scattering, is given by [23,24]

$$\rho(T) = \frac{\pi D^2}{g_s g_v e^2 \hbar \rho_m v_F^2 v_{ph}^2} k_B T, \quad (1)$$

where D , v_{ph} , v_F , and ρ_m are the deformation potential, phonon velocity, Fermi velocity of graphene, and atomic mass density, respectively. g_s (g_v) are the spin (valley) degeneracy. For pristine graphene, $\rho_m = 7.6 \times 10^{-7} \text{ kg/m}^2$, $v_{ph} = 2 \times 10^4 \text{ m/s}$, $v_F = 10^6 \text{ m/s}$, and $D \sim 20 \text{ eV}$ yields $d\rho/dT \sim 0.1 \Omega/\text{K}$ [21–23]. Since the phonon spectrum remains relatively invariant in a moiré system [24,36], v_{ph} is assumed to be constant. Therefore, using the above values for D , ρ_m , v_{ph} and the experimentally measured value of $d\rho/dT \sim 8.5 \Omega/\text{K}$, we estimate the renormalized Fermi velocity $v_F \sim 0.1 \times 10^6 \text{ m/s}$. Please note that different values of $D \sim (10\text{--}30) \text{ eV}$ are quoted in theory [23] and even this uncertainty in D cannot explain the nearly two order of magnitude enhancement in $d\rho/dT$. We would also like to mention that temperature broadening and the excitation of carriers across the minigaps could affect the temperature dependence of resistivity. However, in our device, we believe that this would not affect it significantly due to the following reason. The SDP1 and SDP2 peaks are separated by an energy interval of $\sim 25 \text{ meV}$ (see Supplemental Material [29]). We have performed our analysis near the middle of the two secondary peaks, which is $\sim 12 \text{ meV}$ away from SDP1 and SDP2. The estimated widths of the SDP1 and SDP2 were found to be $\sim 1 \text{ meV}$ and $\sim 1.5 \text{ meV}$, respectively (see Supplemental Material [29]), which is less compared to the temperature broadening of $\sim 4.3 \text{ meV}$ at 50 K . This suggests that the temperature broadening effect will be dominant only near the SDP1 and SDP2 in an energy window of $\sim 4 \text{ meV}$, and it will not affect its

significantly near the density regime, where we have performed our analysis. Therefore, we attribute the large $d\rho/dT$ to the suppression of v_F in the reconstructed bands as a plausible explanation. This reduced Fermi velocity, in our device, is not surprising. As discussed earlier, it could be due to the formation of narrow bands, which has been theoretically predicted in doubly aligned graphene devices with hBN. Our result, therefore, hints at a perspective of creating an alternative framework for narrow bands using doubly aligned graphene on hBN devices. Further experimental and theoretical work is desirable to explore the band structure of doubly aligned bilayer graphene devices and to explore the possibility of obtaining flat dispersion, which could be an interesting platform to study strong interaction physics or superconductivity as observed in twisted bilayer graphene [13].

V. CONCLUSION

In summary, we have presented the electrical and magnetotransport properties of a doubly aligned hBN/BLG/hBN moiré heterostructure. We observe the appearance of strong resistivity peaks due to the presence of two moiré wavelengths. We show that the temperature dependence of resistivity scales linearly with T in the region $n_{s1} < n < n_{s2}$, with a slope that is nearly two orders of magnitude larger than pristine graphene.

ACKNOWLEDGMENTS

The authors would like to acknowledge the Center for Nanoscience and Engineering (CENSE), IISc for fabrication facilities. S.K.S. acknowledges PMRF, MHRD for financial support. A.D. thanks the Department of Science and Technology (DST), India for financial support (Grant No. DSTO-2051) and acknowledges the Swarnajayanti Fellowship (Grant No. DST/SJF/PSA-03/2018-19). A.D. also acknowledges support from the MHRD, Government of India under STARS research funding (Grant No. STARS/APR2019/PS/156/FS).

-
- [1] K. Novoselov, A. Mishchenko, A. Carvalho, and A. C. Neto, 2D materials and van der Waals heterostructures, *Science* **353**, aac9439 (2016).
- [2] M. Yankowitz, J. Xue, D. Cormode, J. D. Sanchez-Yamagishi, K. Watanabe, T. Taniguchi, P. Jarillo-Herrero, P. Jacquod, and B. J. LeRoy, Emergence of superlattice Dirac points in graphene on hexagonal boron nitride, *Nat. Phys.* **8**, 382 (2012).
- [3] M. Yankowitz, Q. Ma, P. Jarillo-Herrero, and B. J. LeRoy, Van der Waals heterostructures combining graphene and hexagonal boron nitride, *Nat. Rev. Phys.* **1**, 112 (2019).
- [4] C. Kumar, S. K. Srivastav, P. Adhikary, S. Banerjee, T. Das, and A. Das, Localization physics in graphene moiré superlattices, *Phys. Rev. B* **98**, 155408 (2018).
- [5] B. Hunt, J. Sanchez-Yamagishi, A. Young, M. Yankowitz, B. J. LeRoy, K. Watanabe, T. Taniguchi, P. Moon, M. Koshino, P. Jarillo-Herrero *et al.*, Massive Dirac fermions and Hofstadter butterfly in a van der Waals heterostructure, *Science* **340**, 1427 (2013).
- [6] C. R. Dean, L. Wang, P. Maher, C. Forsythe, F. Ghahari, Y. Gao, J. Katoch, M. Ishigami, P. Moon, M. Koshino *et al.*, Hofstadter's butterfly and the fractal quantum Hall effect in moiré superlattices, *Nature (London)* **497**, 598 (2013).
- [7] A. Mishchenko, J. Tu, Y. Cao, R. Gorbachev, J. Wallbank, M. Greenaway, V. Morozov, S. Morozov, M. Zhu, S. Wong *et al.*, Twist-controlled resonant tunnelling in graphene/boron nitride/graphene heterostructures, *Nat. Nanotechnol.* **9**, 808 (2014).
- [8] P. Wang, B. Cheng, O. Martynov, T. Miao, L. Jing, T. Taniguchi, K. Watanabe, V. Aji, C. N. Lau, and M. Bockrath, Topological winding number change and broken inversion symmetry in a Hofstadter's butterfly, *Nano Lett.* **15**, 6395 (2015).
- [9] K. Endo, K. Komatsu, T. Iwasaki, E. Watanabe, D. Tsuya, K. Watanabe, T. Taniguchi, Y. Noguchi, Y. Wakayama, Y. Morita *et al.*, Topological valley currents in bilayer graphene/hexagonal boron nitride superlattices, *Appl. Phys. Lett.* **114**, 243105 (2019).

- [10] L. Ponomarenko, R. Gorbachev, G. Yu, D. Elias, R. Jalil, A. Patel, A. Mishchenko, A. Mayorov, C. Woods, J. Wallbank *et al.*, Cloning of Dirac fermions in graphene superlattices, *Nature (London)* **497**, 594 (2013).
- [11] R. Bistritzer and A. H. MacDonald, Moiré bands in twisted double-layer graphene, *Proc. Natl. Acad. Sci. USA* **108**, 12233 (2011).
- [12] Y. Cao, V. Fatemi, A. Demir, S. Fang, S. L. Tomarken, J. Y. Luo, J. D. Sanchez-Yamagishi, K. Watanabe, T. Taniguchi, E. Kaxiras, and P. Jarillo-Herrero, Correlated insulator behaviour at half-filling in magic-angle graphene superlattices, *Nature (London)* **556**, 80 (2018).
- [13] Y. Cao, V. Fatemi, S. Fang, K. Watanabe, T. Taniguchi, E. Kaxiras, and P. Jarillo-Herrero, Unconventional superconductivity in magic-angle graphene superlattices, *Nature (London)* **556**, 43 (2018).
- [14] M. Serlin, C. Tschirhart, H. Polshyn, Y. Zhang, J. Zhu, K. Watanabe, T. Taniguchi, L. Balents, and A. Young, Intrinsic quantized anomalous Hall effect in a moiré heterostructure, *Science* **367**, 900 (2020).
- [15] G. Chen, A. L. Sharpe, E. J. Fox, Y.-H. Zhang, S. Wang, L. Jiang, B. Lyu, H. Li, K. Watanabe, T. Taniguchi *et al.*, Tunable correlated Chern insulator and ferromagnetism in a moiré superlattice, *Nature (London)* **579**, 56 (2020).
- [16] C. Repellin and T. Senthil, Chern bands of twisted bilayer graphene: Fractional Chern insulators and spin phase transition, *Phys. Rev. Research* **2**, 023238 (2020).
- [17] K. Tran, G. Moody, F. Wu, X. Lu, J. Choi, K. Kim, A. Rai, D. A. Sanchez, J. Quan, A. Singh *et al.*, Evidence for moiré excitons in van der Waals heterostructures, *Nature (London)* **567**, 71 (2019).
- [18] L. Wang, S. Zihlmann, M.-H. Liu, P. Makk, K. Watanabe, T. Taniguchi, A. Baumgartner, and C. Schoenenberger, New generation of moiré superlattices in doubly aligned hBN/graphene/hBN heterostructures, *Nano Lett.* **19**, 2371 (2019).
- [19] Z. Wang, Y. B. Wang, J. Yin, E. Tovari, Y. Yang, L. Lin, M. Holwill, J. Birkbeck, D. Perello, S. Xu *et al.*, Composite supermoiré lattices in double-aligned graphene heterostructures, *Sci. Adv.* **5**, eaay8897 (2019).
- [20] M. Anđelković, S. P. Milovanović, L. Covaci, and F. M. Peeters, Double moiré with a twist: Supermoiré in encapsulated graphene, *Nano Lett.* **20**, 979 (2020).
- [21] J.-H. Chen, C. Jang, S. Xiao, M. Ishigami, and M. S. Fuhrer, Intrinsic and extrinsic performance limits of graphene devices on SiO₂, *Nat. Nanotechnol.* **3**, 206 (2008).
- [22] D. K. Efetov and P. Kim, Controlling Electron-Phonon Interactions in Graphene at Ultrahigh Carrier Densities, *Phys. Rev. Lett.* **105**, 256805 (2010).
- [23] E. H. Hwang and S. Das Sarma, Acoustic phonon scattering limited carrier mobility in two-dimensional extrinsic graphene, *Phys. Rev. B* **77**, 115449 (2008).
- [24] F. Wu, E. Hwang, and S. Das Sarma, Phonon-induced giant linear-in- T resistivity in magic angle twisted bilayer graphene: Ordinary strangeness and exotic superconductivity, *Phys. Rev. B* **99**, 165112 (2019).
- [25] L. Wang, I. Meric, P. Huang, Q. Gao, Y. Gao, H. Tran, T. Taniguchi, K. Watanabe, L. Campos, D. Muller *et al.*, One-dimensional electrical contact to a two-dimensional material, *Science* **342**, 614 (2013).
- [26] M. Kuiri, G. K. Gupta, Y. Ronen, T. Das, and A. Das, Large Landau-level splitting in a tunable one-dimensional graphene superlattice probed by magnetocapacitance measurements, *Phys. Rev. B* **98**, 035418 (2018).
- [27] M. Kuiri and A. Das, Energetics of the complex phase diagram of a tunable bilayer graphene probed by quantum capacitance, *Phys. Rev. B* **99**, 125411 (2019).
- [28] C. Kumar, M. Kuiri, J. Jung, T. Das, and A. Das, Tunability of $1/f$ noise at multiple Dirac cones in hBN encapsulated graphene devices, *Nano Lett.* **16**, 1042 (2016).
- [29] See Supplemental Material at <http://link.aps.org/supplemental/10.1103/PhysRevB.103.115419> for details on device characterization, supermoiré features, and temperature dependence for the electron side. The Supplemental Material contains Refs. [20,34].
- [30] G. Chen, M. Sui, D. Wang, S. Wang, J. Jung, P. Moon, S. Adam, K. Watanabe, T. Taniguchi, S. Zhou *et al.*, Emergence of tertiary Dirac points in graphene moiré superlattices, *Nano Lett.* **17**, 3576 (2017).
- [31] A. M. DaSilva, J. Jung, S. Adam, and A. H. MacDonald, Transport and particle-hole asymmetry in graphene on boron nitride, *Phys. Rev. B* **91**, 245422 (2015).
- [32] S. A. Hartnoll, Theory of universal incoherent metallic transport, *Nat. Phys.* **11**, 54 (2015).
- [33] C. R. Dean, A. F. Young, I. Meric, C. Lee, L. Wang, S. Sorgenfrei, K. Watanabe, T. Taniguchi, P. Kim, K. L. Shepard *et al.*, Boron nitride substrates for high-quality graphene electronics, *Nat. Nanotechnol.* **5**, 722 (2010).
- [34] E. H. Hwang and S. Das Sarma, Insulating behavior in metallic bilayer graphene: Interplay between density inhomogeneity and temperature, *Phys. Rev. B* **82**, 081409(R) (2010).
- [35] H. Polshyn, M. Yankowitz, S. Chen, Y. Zhang, K. Watanabe, T. Taniguchi, C. R. Dean, and A. F. Young, Large linear-in-temperature resistivity in twisted bilayer graphene, *Nat. Phys.* **15**, 1011 (2019).
- [36] Y. W. Choi and H. J. Choi, Strong electron-phonon coupling, electron-hole asymmetry, and nonadiabaticity in magic-angle twisted bilayer graphene, *Phys. Rev. B* **98**, 241412(R) (2018).